© 2024 Samuel Frederick

IDEALIZED PARTICLE-RESOLVED LARGE-EDDY SIMULATIONS TO EVALUATE THE IMPACT OF EMISSIONS SPATIAL HETEROGENEITY ON CCN ACTIVITY

BY

SAMUEL FREDERICK

THESIS

Submitted in partial fulfillment of the requirements
for the degree of Master of Science in Climate, Meteorology, and Atmospheric Sciences
in the Graduate College of the
University of Illinois Urbana-Champaign, 2024

Urbana, Illinois

Master's Committee:

Professor Nicole Riemer
Professor Matthew West
Professor Larry Di Girolamo

Abstract

Aerosol-cloud interactions remain a large source of uncertainty in climate models due to complex, nonlinear processes that alter aerosol properties and the inability to represent the full compositional complexity of aerosol populations within large-scale modeling frameworks. The spatial resolution of these models (typically 10-100 km) is often coarser than the spatially varying emissions in the modeled geographic region. This results in diffuse, uniform emission of primary aerosol and gas-phase species instead of spatially heterogeneous concentrations. Aerosol processes such as gas-particle partitioning and coagulation are concentration-dependent, and thus the representation of spatially heterogeneous emissions impacts aerosol aging and properties. This includes climate-relevant quantities like particle hygroscopicity and cloud condensation nuclei (CCN) activity.

This thesis investigates the impact of emissions spatial heterogeneity on CCN activity by using the particle-resolved model PartMC coupled to the Weather Research and Forecasting model configured for large-eddy simulations (LES). The resulting modeling framework resolves turbulence-chemistry interactions and aerosol aging on a per-particle scale. The sensitivity of CCN activity to emissions spatial heterogeneity is evaluated for primary aerosol and gas-phase emissions typical of urban regions. The pattern of emissions is varied to investigate a range of spatially heterogeneity scenarios. For each scenario, CCN activity is compared against a uniform emissions base case to determine the impact of spatially heterogeneous emissions.

TODO: update! We find that CCN concentrations decrease by as much as 10% with increasing emissions spatial heterogeneity, especially for low supersaturations (S=0.1, 0.3%). This work is a first of a kind application of high resolution, particle-resolved LES for quantifying structural uncertainty of CCN activity due to the representation of emissions spatial heterogeneity.

Acknowledgments

Table of contents

List of Tables . . . . . **vi**

List of Figures . . . . . **vii**

Chapter 1 Introduction **1**
1.1 The complexity of aerosols and environmental feedbacks 1
1.2 Spatial heterogeneity of aerosols 3
1.3 Impacts of aerosols on climate 4
1.4 Treatment of aerosols across modeling frameworks 5
1.5 Objectives of this thesis 6

Chapter 2 Quantifying emissions spatial heterogeneity and mixing **8**
2.1 Existing Approaches to Quantifying Spatial Heterogeneity 8
2.1.1 Spatial autocorrelation and semivariograms 9
2.1.2 Fractal dimensions 9
2.1.3 Lacunarity 9
2.1.4 Information entropy based metrics 10
2.1.5 Nearest neighbor statistics for point-based heterogeneity 10
2.1.6 Multiscale norms 11
2.2 Metrics for quantifying the mixing of reactive compounds 11
2.2.1 Segregation intensity 11
2.2.2 Damköhler number 12
2.3 A novel approach to quantifying spatial heterogeneity 13
2.3.1 Metric definition 14
2.3.2 Computational methods for computing the spatial heterogeneity metric 15
2.3.3 Example calculations for emission patterns 18

Chapter 3 Modeling tools **19**
3.1 Large-eddy simulations 19
3.1.1 Sub-grid scale parameterizations 20
3.1.2 Computational domain 21
3.1.3 Meteorological Initial Conditions 22
3.1.4 Simulation spin-up 23
3.2 Gas phase simulations 24
3.2.1 Chemical mechanism 24
3.2.2 Initial conditions and emissions 25
3.3 Multiphase simulations 26
3.3.1 Chemical mechanism 26
3.3.2 Aerosol representation 26
3.3.3 Initial conditions and emissions 27

Chapter 4 Impacts of emissions spatial heterogeneity on gas-phase reactions **30**

Chapter 5 Impacts of emissions spatial heterogeneity on aerosol properties in a particle resolved framework **31**

Chapter 6 Conclusions **32**

References **33**

List of Tables

1.1 Table to test captions and labels. 6

3.1 Gas phase emissions and initial conditions. Table taken from N. Riemer et al. 2009 with permission. 25

3.2 Aerosol emissions and initial conditions. Table taken from N. Riemer et al. 2009 with permission. 28

List of Figures

1.1 Cartoon representation of a particle resolved model 7

2.1 Dependence of the Damköhler number on turbulent and reactive timescales. Figure adapted from V. Rao Kotamarthi and Yan Feng, Argonne presentation, STM meeting 2017. 13
2.2 Example subsets for *SH* calculation. (a) Full domain mean. (b-f) Examples of rectangular subsets (highlighted regions) over which the subset mean is computed. 15
2.3 Compute time for the naive looping *SH* Fortran subroutine. The x-axis indicates the total number of domain grid cells (elements) in the array passed to the function. A power law regression is plotted as the red dashed line. 16
2.4 Compute time for the Monte Carlo *SH* Fortran subroutine. The x-axis indicates the number of domain subsets that are randomly selected to determine the *SH* estimate. A power law regression is plotted as the red dashed line. 17
2.5 *SH* estimate in blue for the Monte Carlo sampling subroutine vs. the number of randomly selected domain subsets (top panel). The true value of *SH* computed via the naive algorithm is shown as the black line. Absolute relative error between *SH* estimate and the true value of *SH* (middle panel). Bias between *SH* estimate and the true value of *SH* (bottom panel) . . . 18

3.1 Idealized atmospheric sounding used for domain meteorological initial conditions. Initial conditions for potential temperature (left) and specific humidity (right). TODO: check what is best, units in brackets or in paretheses? Figure 3.2 uses brackets so I should be consistent either way... 22
3.2 Resolved-scale vertical heat flux profiles (left) and TKE at intervals of 10 minutes during the first hour of simulation spin-up. 23
3.3 Aerosol initial condition size distributions. 29
3.4 Aerosol emission size distributions. 29

Chapter 1

Introduction

This chapter discusses fundamental properties of aerosols and computational modeling techniques which motivate this thesis. A description of atmospheric aerosols and the challenges associated with capturing the complexity of aerosol properties and their environmental feedbacks is discussed. Additionally, numerical modeling treatments for aerosols are presented along with approaches to improve the characterization of aerosol complexity. Finally, research questions are presented which outline primary avenues of inquiry for this thesis.

1.1 The complexity of aerosols and environmental feedbacks

An aerosol is a collection of particles composed of one or more chemical species that are suspended in a fluid or gas. In the atmosphere, aerosol particles vary considerably in terms of their physical properties such as size, composition, and origin. Additionally, the chemical, thermodynamic, and radiative properties of aerosol particles can alter the state of the aerosol and the surrounding environment through numerous feedback mechanisms. In turn, aerosol particles exhibit a complex, non-linear coupling with the environment that spans broad spatial and temporal scales.

Aerosol particles are typically measured by their diameter where spherical morphology is assumed. The smallest particles have diameters on the order of 1 nm and are produced via the nucleation of low-volatility vapors. On the opposite extreme of particle sizes, the largest particle diameters can exceed 100 μm. In total, aerosols span approximately five orders of magnitude. To capture the broad scale of particle diameters that may be present in a population of aerosol particles, aerosol size distributions often represent the number concentration of particles as a function of the logarithm of particle diameter. The particle size distribution may be represented by multiple modes—lognormal size distributions—that are differentiated by the characteristics of particles within each mode, including growth and removal mechanisms. Typically, three distinct modes are

present in a particle size distribution: the nucleation, accumulation, and coarse mode.

Nucleation mode particles are up to 20 nm in diameter and undergo rapid growth as gas-phase species condense onto the particle surface or as particles inelastically collide through coagulation. They are removed from the nucleation mode by growth within XX time into the accumulation mode, which spans particle diameters from 0.1 μm to 2 μm . In addition to particles that enter the accumulation mode through growth by condensation or coagulation, particles may be released directly into the accumulation mode via primary emissions. Removal mechanisms such as wet and dry deposition are least efficient in the accumulation mode, allowing particles to remain suspended in the atmosphere for days to weeks. Particles in the coarse mode have diameters exceeding 2 μm and are produced by mechanical processes such as abrasion and the resuspension of dust. Due to their size, particles in the coarse mode are rapidly removed by gravitational settling within minutes to hours. This multi-modal description of the aerosol size distribution points to the inherent complexity of aerosol population dynamics—production, growth, and removal mechanisms differ considerably by particle size.

As noted, production mechanisms vary across aerosol modes (e.g., nucleation of low-volatility vapors, emission of primary aerosol into the accumulation mode, resuspension of coarse particles, etc.). These processes typically involve different chemical species. For example, whereas volatile organic compounds (VOCs) such as isoprene and other organic carbon (OC) species may undergo oxidation reactions which lower their volatility and promote particle nucleation, particles released directly into the accumulation or coarse mode as primary aerosol may consist of either organics that are produced during combustion such as black carbon (BC) or inorganics such as sea salt spray, mineral dust, [other species]. Here its worth acknowledging contribution of precursor emissions to chemical aging, secondary production of aerosol-phase matter, changes to aerosol mixing state, etc.. As a result, aerosol particles are compositionally diverse.

In addition to diversity in the composition of aerosol particles across the size distribution, aerosol populations also exhibit spatiotemporal variations which alter the local structure and composition of the aerosol. The geographic distribution of emission sources, varied land use, and topography lead to spatial heterogeneities in the emission of gas-phase precursors and primary aerosols. Additionally, temporal trends alter the meteorological state of the atmosphere and the concentration of reactive gas or aerosol-phase species. For instance, diurnal variation in the structure of the boundary layer due to surface heating determines the strength of vertical transport and mixing of primary aerosol or reactive gas-phase species. [Could talk about photolysis]. Furthermore, the timing of emissions may play a crucial role in determining whether a chemical

reaction will take place; reactive species must be present in the same space and time to undergo reaction.

Seinfeld and Pandis 1998

1.2 Spatial heterogeneity of aerosols

- Spatial heterogeneity of surface heterogeneities impacts the evolution of the atmospheric state
  - Joint modeling and observation based studies like Fast et al. 2019 "HI-SCALE" heterogeneities in soil moisture were critical to cloud structure and the development of deeper convecting clouds. Modeling studies showed that under scenarios with smoothly varying soil moisture, clouds did not develop into open cell, deep convective cumulus capable of precipitating and instead were characterized by shallow, uniform non-precipitating clouds.
  - Lee et al. 2018 conducted an idealized LES study in which surface heat fluxes (including both sensible and latent heat flux) were prescribed by checkerboard patterns of ranging spatial heterogeneity (most heterogeneous being the lowest frequency checkerboard pattern–largest pattern length scale–and least heterogeneous being the highest frequency patterns–smallest pattern length scale). They found that secondary circulation developed under scenarios with the highest spatial heterogeneity and minimal background winds (less than 2 $\mathrm{m\,s^{-1}}$). This circulation was responsible for transporting moisture from checkerboard regions with greater latent heat flux to drier regions with lesser latent heat flux.
- Aerosols have shown to also be highly variable:
  - Examples: Urban, rural, maritime, etc. (variability in composition, concentration). See Seinfeld and Pandis for some discussion of typical conditions in each region.
- Existing studies looking at spatial heterogeneity of aerosols
  - Fast et al. 2022 (properties)
  - Hassan et al. 2023 (emissions)
  - Franklin et al. 2018
- Impacts on aerosol processes: non-linear, concentration dependent processes

  - Coagulation
  - Chemistry
    * Present body of literature investigates predominantly gas-phase chemistry (e.g., isoprene-OH reaction) and contribution of chemical segregation due to turbulence and spatial distribution of reactive species
  - These processes alter the radiative and hygroscopic properties of the aerosol
- Representation of aerosol spatial heterogeneity in models
  - Lack of resolution, impact of sub-grid scale variability on aerosol properties (Radiative properties, CCN concentrations)
    * Lin et al. 2017 find that aerosol (mass I think) SGV over the pacific ocean within a typical GCM grid cell is 15% near the surface and as high as 50% in the free troposphere. (this could also be cited in the paragraph above on variability of aerosols).
    * Weigum et al. 2016 look at the effect of SGV on AOD and CCN by comparing WRF-Chem runs at 80 km resolution against 10 km resolution and find an underestimation of AOD by 13% and an overestimation of CCN by 27%. They find gas-phase chemistry and aerosol water uptake are processes which are most affected.
    * Qian et al. 2010 (study over mexico, contribution of emissions to SGV)
    * Gustafason et al. 2011 (similar to Qian 2010, radiative effects)
    * Crippa et al. 2017
  - Attempts at parameterizations (adaptive grids, plume in grid modeling, coagulation parameterizations, PDF-based methods, stochastic fields, etc.)

1.3 Impacts of aerosols on climate

- Aerosol-radiative effects
  - Absorption and scattering of radiation alters the stability of the atmosphere due to warming/cooling

  - Aerosols alter large scale circulation. For example, higher aerosol concentrations due to anthropogenic activity in the northern hemisphere results in global-scale heterogeneity. Fan et al. 2016 (via Ming and Ramaswamy 2011) note that this weakens the northern branch of the Hadley circulation, resulting in an energy flux from the southern hemisphere towards the north.

- Aerosol-cloud interactions
  - Indirect effects - Twomey, etc.
  - Impacts on cloud type and evolution
    * Warm rain mechanism well understood
    * Thermodynamic invigoration due to increased CCN for deep-convective clouds (mechanism much more complicated, still contested)
    * Have been shown to promote formation of open cells
  - Radiative forcing due to ACI and sources of uncertainty
    * One source of uncertainty is aerosol representation in models

1.4 Treatment of aerosols across modeling frameworks

- Simplified bulk, modal, sectional treatments
  - Use in regional, global scale models
  - Consequences of simplified treatment on representation of CCN concentrations, etc.
- Particle resolved aerosol modeling
- Transport representation
  - Large scale models use RANS and thus cannot resolve turbulence and associated heterogeneities in gas, aerosol concentrations
  - LES - adoption for modeling aerosols is still nascent, some examples like UCLALES-SALSA, DALES have been used to evaluate aerosol-cloud interactions, but none leverage a high-resolution particle resolved aerosol treatment

1.5 Objectives of this thesis

- Primary science questions
  - Impacts of emissions spatial heterogeneity on aerosol processes (e.g., coagulation, chemistry, etc.)?
  - Impacts of emissions spatial heterogeneity on aerosol properties (e.g., composition, concentration, hygroscopicity)?
  - How is the impact of spatial heterogeneity on aerosols modulated by changes to the composition of emissions?
  - How does emissions spatial heterogeneity alter the activity of CCN?
- Development of a framework for evaluating spatial heterogeneity impact on aerosol properties, including CCN activity
  - Transport vs. aerosol treatment graph
  - Future extension could quantify the structural uncertainty for the representation of aerosols (properties, ccn activity, etc.) in coarser resolved models such as regional and global scale models that use modal/sectional aerosol treatments and parameterize turbulence

Col1	Col2	Col2	Col3
1	6	87837	787
2	7	78	5415
3	545	778	7507
4	545	18744	7560
5	88	788	6344

Table 1.1: Table to test captions and labels.

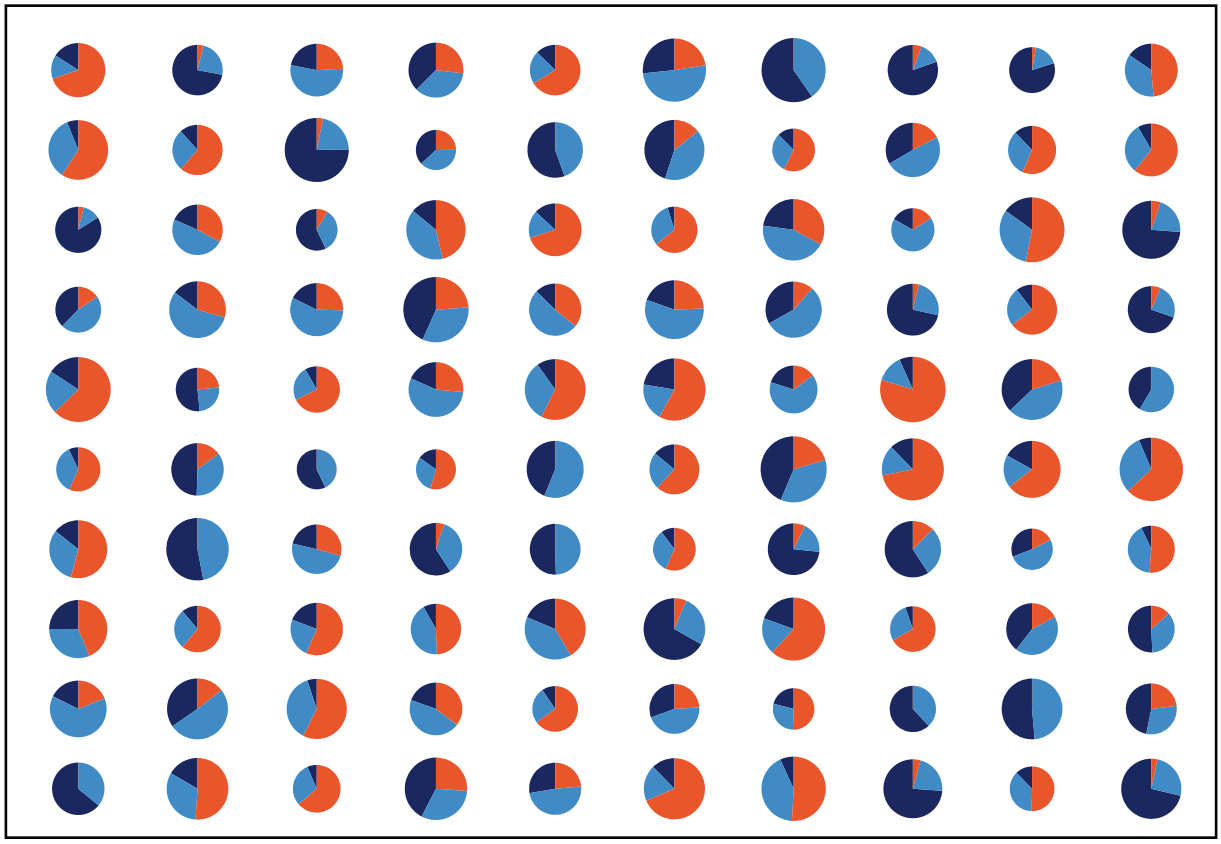

Figure 1.1: Cartoon representation of a particle resolved model

Chapter 2

Quantifying emissions spatial heterogeneity and mixing

This chapter provides an overview of spatial heterogeneity (SH) and its relevance to quantifying the spatial variability of atmospheric emissions. We begin with a brief discussion of cross-disciplinary efforts to quantify SH. We then narrow our focus to quantifying the heterogeneity and mixing of reactive compounds in the atmosphere and characterize the gap in existing approaches that necessitate the development of a new, generally applicable SH metric that we will use in this thesis. The remainder of this chapter is dedicated to discussing our novel SH metric, the development of a Monte-Carlo based method for efficiently computing the metric over large domains, and its application to measuring the SH of idealized 2D patterns.

2.1 Existing Approaches to Quantifying Spatial Heterogeneity

SH is ubiquitous across the natural sciences ranging from ecology to atmospheric sciences. SH plays an important role in biological diversity, human land use and associated environmental feedbacks, and drives changes in atmospheric dynamics through spatially varying surface fluxes of heat, water vapor, and emissions. Despite its importance, quantifying SH is challenging in part because its definition can be highly dependent on the end use case. For instance, a metric used in geostatistics for measuring geographic variability in land use may not be particularly useful to an ecologist concerned with how spatially dependent a species population is on surrounding resources. Furthermore, mathematical assumptions central to the choice of metric such as scale similarity may not be applicable across use cases and thus limit the metrics' applicability. This has prompted the development of numerous metrics across disciplines that quantify SH. Here, we discuss various prominent SH metrics that range in applicability and complexity, and point to limitations in these approaches for use in quantifying emissions spatial heterogeneity.

2.1.1 Spatial autocorrelation and semivariograms

Spatial correlation between measurements can be evaluated using correlograms and semivariograms. Correlograms are created by computing the correlation, measured via Pearson's correlation coefficient, between two measurements separated by a given distance. Once the correlation across all distances and associated measurement pairs is computed, correlation is plotted against distance. A similar approach is employed for semivariograms, where the variance is plotted against distance between measurement pairs. Cooper et al. 1997 apply these techniques to determine the spatial correlation in streams between snail density and algal biomass, which serves as an important microhabitat. The authors show how these metrics can be leveraged to quantify the spatial correlation and variability between measurements. While correlograms and semivariograms are useful for explaining the correlation and variance between spatially distributed measurements, they do not provide a one-point statistical measure of how spatially heterogeneous a region is, nor do they provide information on how variance for a quantity of interest is spatially arranged over a region.

2.1.2 Fractal dimensions

A Fractal dimension, or fractional dimension, is a non-integer dimension (Mandelbrot 1967, 1982). Surfaces with greater complexity across spatial scales have higher fractal dimensions and vice versa. Fractal dimensions are scale invariant, meaning that it can be used to evaluate heterogeneity across surfaces of varying area. Loke and Chisholm 2022 discuss their use in ecology and point to numerous important limitations and considerations when utilizing fractal dimensions. The authors note that in practice, measuring fractal dimensions is challenging due to the need to quantify the broad range of scales which may be limited by the resolution of measurement techniques. Additionally real-world objects and surfaces are not truly fractal because self-similarity breaks down at certain scales.

2.1.3 Lacunarity

Surfaces with similar fractal dimensions can have dissimilar variations or texture (i.e., their variance can be arranged in different ways). This led Mandelbrot (1983 or 1982?) to introduce Lacunarity as a metric for quantifing the textural variation of surfaces with similar fractal dimension. Lacunarity is related to the distribution of scales of texture in a surface. Surfaces with a broader range of texture, including large and small gaps and variations, will tend to have high lacunarity. For more homogeneous objects, the distribution

of texture scales will be narrower and will result in a lower lacunarity value. Dong 2000 provide an overview of lacunarity and its use in geography and geographic information science (GIS) applications. They note that lacunarity is often quantified using a gliding box algorithm, for which the researcher must choose the gliding box size. Importantly, changes to the gliding box size do not ensure linear scaling of the difference between lacunarity of multiple patches, meaning that, for instance, a patch may have higher lacunarity compared to other patches at small gliding box sizes but may have lower lacunarity than other patches at larger gliding box size. While this may be a useful attribute of lacunarity if one wishes to evaluate the scale dependence of spatial variability and the scales at which patches appear spatially similar or dissimilar (indeed, this is a primary use case as outlined by Dong 2000), gliding box size introduces an additional parameter one one must choose when quantifying spatial heterogeneity and could complicate intercomparison of lacunarity measurements.

2.1.4 Information entropy based metrics

In landscape ecology, information entropy based metrics such as Shannon's evenness index are used to quantify the patchiness of topography that is divided among numerous land uses classes. Plexida et al. 2014 evaluate a number of metrics, including Shannon's evenness index, for measuring the topological variability and land use of central Greece. For its use in landscape ecology, Shannon's evenness quantifies how evenly distributed the various land use types in a region are. It is defined as Shannon's diversity index over N populations (i.e., the Shannon entropy) divided by the maximum diversity index. Shannon's eveness index is useful if evaluating a region with numerous patches that are divided into different categories; however, its use is less apparent for quantifying the spatial heterogeneity of a single scalar field.

2.1.5 Nearest neighbor statistics for point-based heterogeneity

Shu et al. 2019 discuss nearest neighbor distance statistics for use in GIS settings to quantify the spatial heterogeneity of points and apply various metrics to example cases including the spatial distribution of crime events in a city, regional seismic activity in Yutian China, and taxi routes in Beijing China. These examples range from 2D to 4D, illustrating the multidimensional applicability of nearest-neighbor metrics. The authors present a goodness-of-fit metric based on the distribution of nearest neighbor distances called the level of heterogeneity. A normalized version of the metric is proposed to resolve issues that arise when comparing datasets with differing magnitudes due to differences in scale or intensity. The authors note that while

the proposed metric is suitable for capturing point-based spatial heterogeneity, it is quite computationally expensive. It is recommended that alternative nearest-neighbor metrics evaluated alongside the proposed metric should be preferred for computationally intensive datasets.

2.1.6 Multiscale norms

Sobolev norms have been used to quantify the mixing and transport of passive scalars in fluids (Thiffeault 2012). Sobolev norms act as a weighted sum of the Fourier coefficients resulting from the Fourier transform of a scalar field (i.e, the passive scalar suspended in either a fluid or the atmosphere). The multiscale nature of Sobolev norms refers to the selection of Sobolev space H^q over which the norm is defined. Thiffeault 2012 show that the choice of Sobolev norm for $q < 0$ is valuable for flow mixing applications as the magnitude of the norm decays alongside the mixing of the medium.

2.2 Metrics for quantifying the mixing of reactive compounds

Atmospheric constituents that undergo chemical reactions including gas phase and aerosol species are subject to both spatial and temporal constraints that determine the rate at which reactions will proceed. For instance, species must be spatially collocated for reactions to occur, and they must remain in close proximity over the timescale that a given reaction will proceed. This gives rise to two important metrics: (1) segregation intensity, which quantifies the spatial proximity of reactive species and (2) the Damköhler number, which characterizes the dominant timescales governing the reactivity of species.

2.2.1 Segregation intensity

The segregation intensity, first theorized by Danckwerts 1952 for use in combustion processes, is a measure of how spatially segregated or mixed two reactive species are that follow a typical second-order reaction of the form

$$\mathrm{A} + \mathrm{B} \longrightarrow \mathrm{C}. \tag{2.1}$$

Using Reynolds decomposition to express each species concentration as the sum of a spatial average and local deviation, $[A] = \overline{[A]} + [A]'$, $[B] = \overline{[B]} + [B]'$, such that the chemical reaction proceeds as

$$\frac{d[A]}{dt} = \frac{d[B]}{dt} = -k\left(\overline{[A]} \cdot \overline{[B]} + \overline{[A'][B']}\right). \tag{2.2}$$

The segregation intensity is then

$$I_s = \frac{\overline{[A'][B']}}{\overline{[A]} \cdot \overline{[B]}}, \tag{2.3}$$

such that the chemical reaction can be expressed as

$$\frac{d[A]}{dt} = \frac{d[B]}{dt} = -k\left(\overline{[A]} \cdot \overline{[B]}\right)(1 + I_s). \tag{2.4}$$

Thus, I_s can be thought of as imposing an effective reaction rate $k^{\text{eff}} = k(1 + I_s)$. When $I_s = -1$, species A and B are fully spatially separated, such that no reaction occurs. As I_s approaches zero, the two species become fully mixed and the effective reaction rate matches the ideal rate of reaction. I_s can also be positive, corresponding to positive covariance between species which effectively increases the rate of reaction.

2.2.2 Damköhler number

The Damköhler number (Damköhler 1947) relates the turbulence and chemical reaction timescales via the ratio

$$D_a = \frac{\tau_{\text{turb}}}{\tau_{\text{chem}}}. \tag{2.5}$$

The definition of turbulent and chemical timescales varies by application. For the convective boundary layer, Vinuesa and Arellano 2003 adopt the following expression for the Damköhler number,

$$D_a = \frac{z_i}{w_*} k[B], \tag{2.6}$$

where w_* is the velocity scale in the convective boundary layer and is defined as $\left[(g/\Theta_v)\overline{w\theta}_0 z_i\right]^{1/3}$, and where g is gravitational acceleration, Θ_v is virtual potential temperature, $\overline{w\theta}_0$ is vertical heat flux, and z_i is the boundary layer height.

Figure 2.1 displays the three primary regimes for the Damköhler number that determine the abundance of precursor concentrations $[A]$ and $[B]$. When the turbulent and chemical timescales are balanced, $D_a = 1$. If

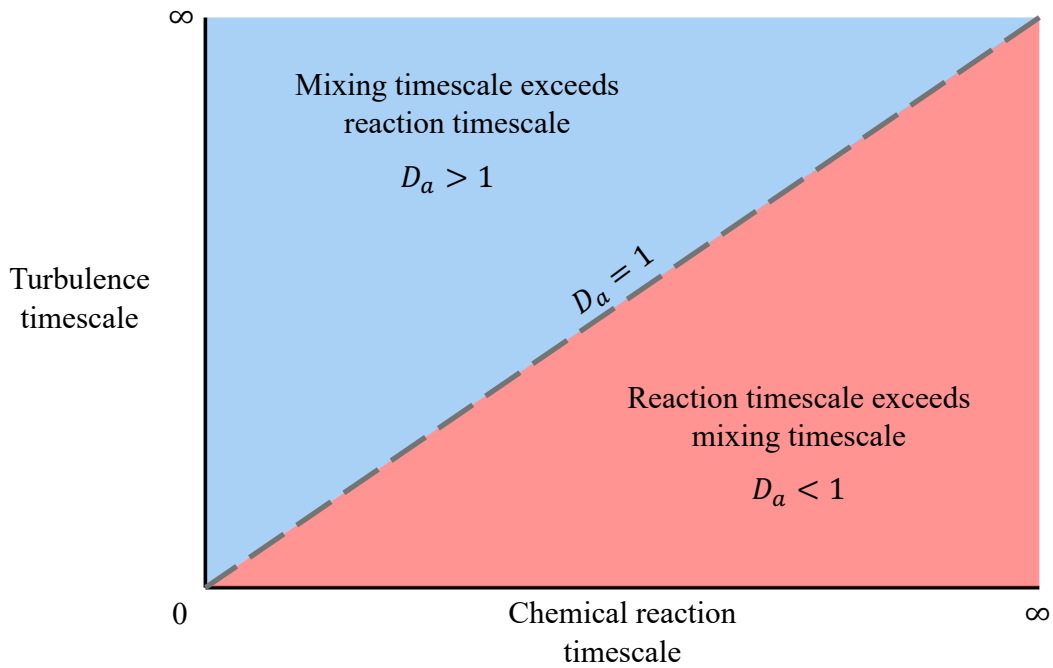

Figure 2.1: Dependence of the Damköhler number on turbulent and reactive timescales. Figure adapted from V. Rao Kotamarthi and Yan Feng, Argonne presentation, STM meeting 2017.

the chemical reaction timescale is shorter than the turbulence timescale, $D_a > 1$ and the concentration of the precursors will be determined by the rate at which turbulence mixes the reactive compounds (fast-chemistry regime). Conversely, if the chemical reaction timescale is slower than the turbulent timescale, $D_a < 1$ such that the concentration of precursors is determined by the rate of chemical reaction (slow-chemistry regime). Thus, the Damköhler number indicates the relative importance of turbulence in chemical reactions – in the fast chemistry regime with reactions with $D_a > 1$, turbulent scales responsible for mixing the reactive compounds should be fully resolved. Examples of relevant gas-phase reactions in convective boundary layer that correspond to the fast-chemistry regime include oxidation of volatile organic compounds such as isoprene by OH I assume oxidation of SO2 by OH as well?.

2.3 A novel approach to quantifying spatial heterogeneity

Existing approaches to quantifying spatial heterogeneity discussed in Section 2.1 and metrics for mixing of reactive compounds in Section 2.2 provide valuable information on the state of a heterogeneously distributed field, however each metric varies in terms of range of applicability, interpretability, and ease of

implementation.

For instance, spatial autocorrelation and semivariograms are relatively easy to interpret and are computationally efficient to measure, but they are primarily useful for capturing the correlation and variability at a single point rather than over an entire region. Alternatively, the nearest neighbor metric proposed by Shu et al. 2019 is useful across a broad range of applications as illustrated by the authors, however, their approach is computationally expensive and is not readily interpretable to the same manner as other spatial heterogeneity metrics. Metrics for mixing provide useful information on how spatially colocated reactive compounds are and the relevant timescales that determine the abundance of precursors, however they do not provide information on how the variance in the spatial distribution of each compound is arranged.

Thus, there exists the need for a novel spatial heterogeneity metric for use in atmospheric science applications including quantifying emissions spatial heterogeneity and subsequent atmospheric field heterogeneity once compounds are emitted into the planetary boundary layer. Mohebalhojeh et al. 2024 (in prep) have developed a new approach to measuring spatial heterogeneity with key benefits being that their approach is broadly applicable, straightforward to interpret, and computationally efficient to measure using a Monte Carlo approach discussed in Section **??**.

2.3.1 Metric definition

The spatial heterogeneity metric, subsequently SH, quantifies the level of heterogeneity for single scalar quantity over a 2-dimensional surface. In this thesis, the scalar of interest is either gas phase or aerosol species and the 2-dimensional surface is either the ground level in the case of emissions or a horizontal plane through the computational domain to quantify atmospheric field heterogeneity within the planetary boundary layer.

SH is calculated by summing up the absolute difference between the mean of a scalar quantity over a rectangular subset of the domain and the domain averaged value for all possible subsets. Over a discrete 2-dimensional grid with N cells along the x-axis and M along the y-axis, there exist $P = (N(N-1)+1)(M(M-1)+1)$ total possible rectangular subsets. For a scalar field f defined over some domain S, SH is computed as

$$SH(f,S) = \frac{1}{P}\sum_{\tilde{S}\in\mathbb{R}} |\overline{f}(S) - \overline{f}(\tilde{S})|. \tag{2.7}$$

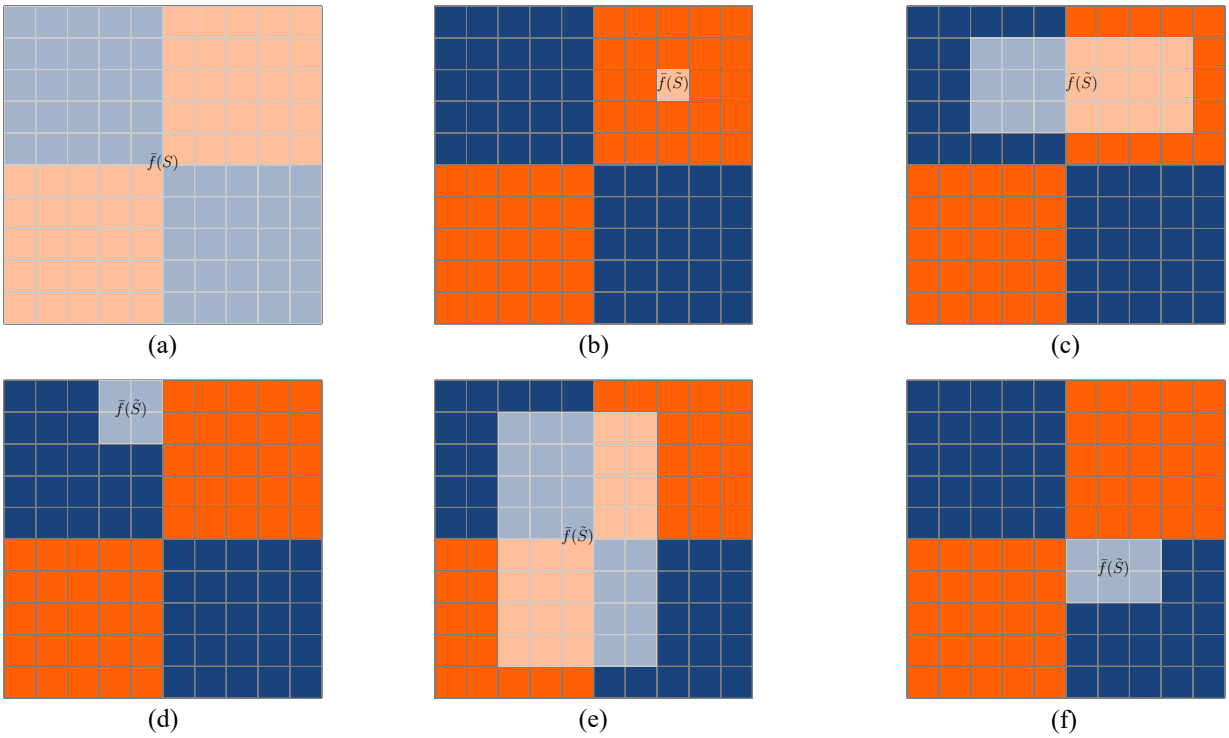

Figure 2.2: Example subsets for *SH* calculation. (a) Full domain mean. (b-f) Examples of rectangular subsets (highlighted regions) over which the subset mean is computed.

Because the range of gas phase and aerosol emissions varies across orders of magnitude, it is useful to instead utilize a normalized version of the spatial heterogeneity metric,

$$SH(f,S) = \frac{1}{\overline{f}(S)\left[\frac{3}{2}(N\times M)(N-1)(M-1)+N(N-1)+M(M-1)\right]}\sum_{\tilde{S}\in\mathbb{R}}|\overline{f}(S)-\overline{f}(\tilde{S})|. \tag{2.8}$$

A visualization of the total domain mean $\overline{f}(S)$ and domain subset means $\overline{f}(\tilde{S})$ are shown in Figure 2.2. The checkerboard pattern represents an idealized emission pattern, where orange-filled cells correspond to regions of uniform emissions and dark blue regions correspond to zero emissions. $\overline{f}(S)$ is shown in subfigure (a), while five examples of rectangular subsets are displayed in subfigures (b-f).

2.3.2 Computational methods for computing the spatial heterogeneity metric

To calculate *SH* over a computational domain, an array comprising the scalar quantity of interest with dimension equal to the size of the domain (N by M) is passed to a Fortran subroutine. Here, we discuss two approaches to calculating *SH*: a computationally expensive naive looping algorithm and a significantly more efficient Monte Carlo based method.

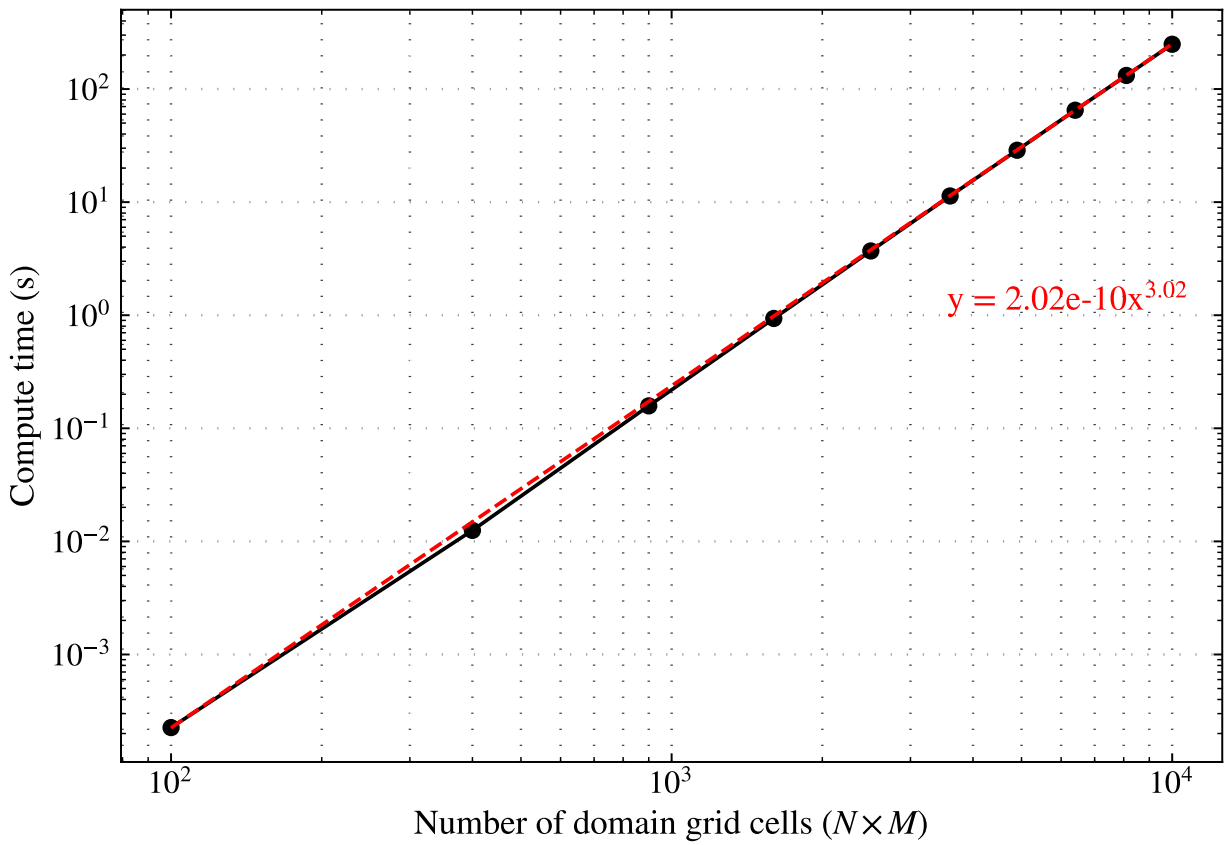

Figure 2.3: Compute time for the naive looping *SH* Fortran subroutine. The x-axis indicates the total number of domain grid cells (elements) in the array passed to the subroutine. A power law regression is plotted as the red dashed line.

The naive subroutine loops over all possible rectangular subdomains which can be quite computationally expensive, especially for domains with a large number of grid cells (e.g., 100×100 grid cells laterally as used for domain mesh size in this thesis). Figure 2.3 shows the computational scaling for a Fortran subroutine using this naive looping algorithm. A power law regression (red dashed lined) is fit to the compute time vs. the total number of domain grid cells. The naive looping algorithm scales as $O(n^3)$ for n the number of grid cels. For domain sizes used in this thesis ($N = M = 100$), this results in a single calculation taking in excess of 2 minutes.

Instead of looping over every possible subdomain, we may use the fact that the probability of selecting any given subdomain is the same (i.e., the sampling probability is uniform across the entire domain) in order to construct a Monte Carlo sampling based approach for calculating *SH*. We then pass the array with domain scalar values alongside a parameter for the number of subsets to sample to our Monte Carlo-

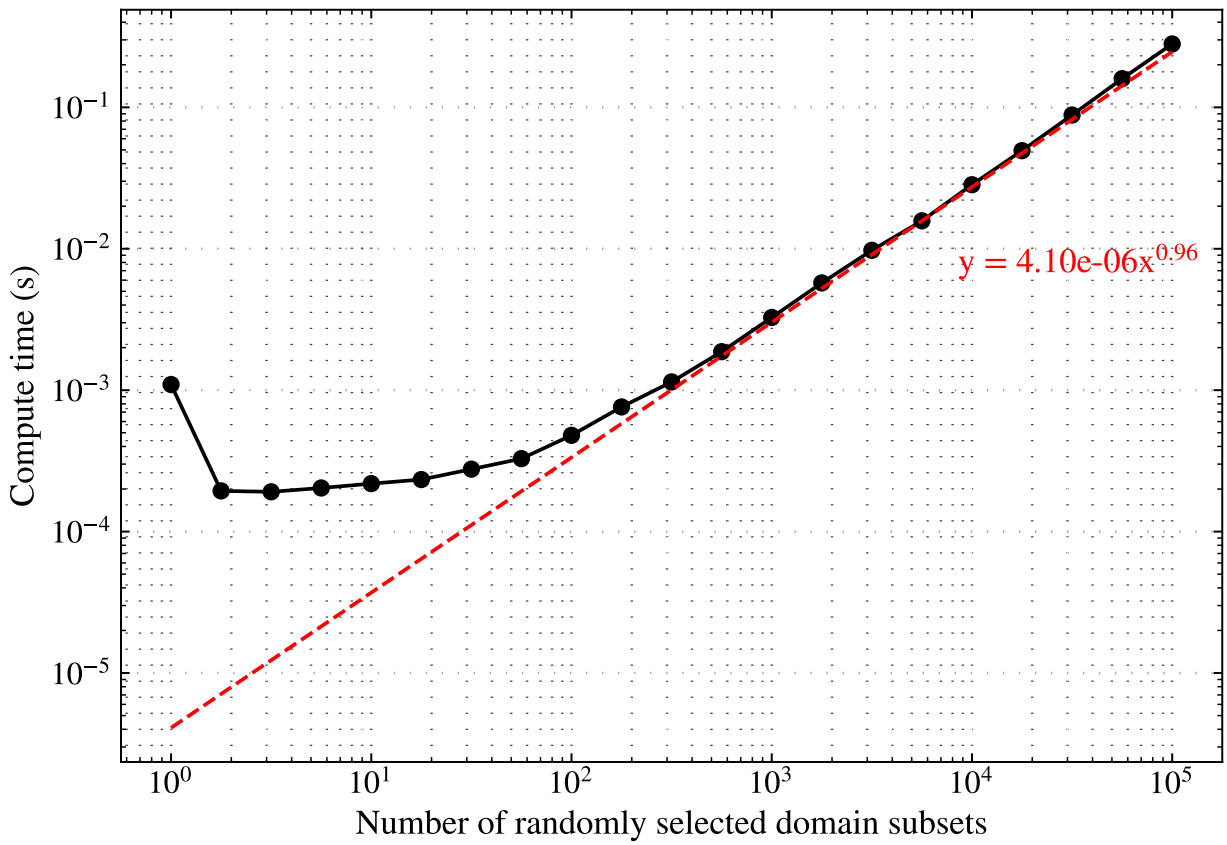

Figure 2.4: Compute time for the Monte Carlo *SH* Fortran subroutine. The x-axis indicates the number of domain subsets that are randomly selected to determine the *SH* estimate. A power law regression is plotted as the red dashed line.

based Fortran subroutine. Figure 2.4 shows the compute time for corresponding number of randomly selected domain subsets, ranging from 1 to 100,000 for a domain with dimensions $N = M = 100$ and $P = (100(100-1)+1)(100(100-1)+1) = 98,029,801$ total subsets. For a low number of randomly selected subsets (number of subdomains $\lesssim 100$), the algorithm scales quite weakly, suggesting that computational overhead limits speedup in this region over the naive algorithm. As the number of subdomains increases above 100, the algorithm scales as $O(S)$ for $S \subset P$ as indicated by the power law regression.

We validate the accuracy of the Monte Carlo sampling subroutine against the naive looping approach in Figure 2.5. First, the precise value of *SH* was computed via the naive algorithm for a scalar field of random noise with dimensions $N = M = 100$. We then vary the number of randomly selected subsets used to compute the estimate of *SH* in the Monte-Carlo subroutine. The top panel in Figure 2.5 shows how the *SH* estimate converges on the precise value of *SH* (shown as a black line). The middle panel displays the relative error between *SH* estimates and the precise value (note the logarithmic scaling). Relative error appears to

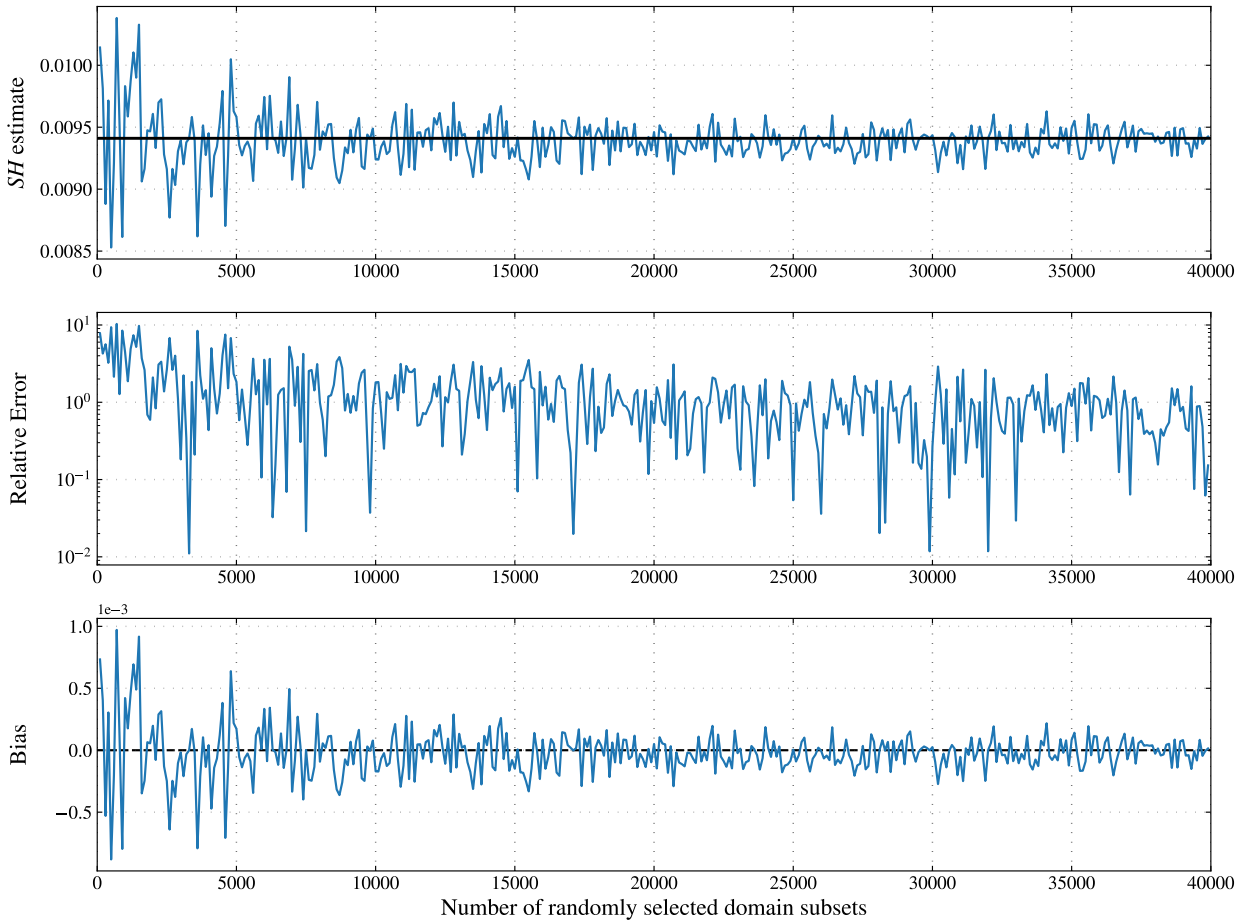

Figure 2.5: *SH* estimate in blue for the Monte Carlo sampling subroutine vs. the number of randomly selected domain subsets (top panel). The true value of *SH* computed via the naive algorithm is shown as the black line. Absolute relative error between *SH* estimate and the true value of *SH* (middle panel). Bias between *SH* estimate and the true value of *SH* (bottom panel)

plateau around $\sim 1\%$ as the number of randomly selected domain subsets approaches 40,000. This suggests diminishing returns for accuracy at the expense of computational cost as discussed previously for Figure 2.4. Bias between *SH* estimates and the precise value of *SH* is shown in the bottom panel.

Given the performance of the Monte Carlo sampling subroutine over the naive looping approach and its ability to reach a high level of accuracy with minimal error when sampling a sufficient number of domain subsets, we utilize the Monte Carlo method for subsequent *SH* calculations. For such calculations, we choose the number of randomly selected domain subsets to be 40,000 as this results in relative error $\lesssim 1\%$ for the domain size $N = M = 100$ used in this thesis.

2.3.3 Example calculations for emission patterns

Chapter 3

Modeling tools

This chapter discusses the modeling tools necessary for conducting simulations presented in this thesis. A description of the transport treatment, large-eddy simulations, is provided alongside discussion of requisite sub-grid scale parameterizations that we utilize. Attributes of the computational domain, including its spatial extent, grid resolution, and other defining qualities are presented. Meteorological initial conditions for simulations are discussed as well as determination of necessary spin-up time for the development of convective boundary layer in the computational domain. Subsequently, chemical mechanisms used for gas phase and aerosol chemistry are discussed. Lastly, the aerosol model, PartMC, and its coupling with the chosen transport model is discussed.

3.1 Large-eddy simulations

Within the planetary boundary layer (PBL), turbulent eddies are responsible for mixing and transporting gases and aerosol particles as well as thermal and kinetic energy. Over time, these eddies break down due to flow instabilities, frictional losses due to interactions with physical boundaries, and the viscosity of the atmospheric constitutents. Therefore, it is important for modeling frameworks that represent the PBL to explicitly resolve the physical scales over which transport and mixing occur, as well as accurately model the dynamical tendency of kinetic energy transfer from large to small eddies.

Representation of turbulence in modeling frameworks is a computationally challenging task because of the range of scales one must consider and the associated need for high spatial resolution. In the PBL, turbulent eddies range in size from hundreds of meters (check this) to the Kolmogorov length scale on the order of 1 mm (check this, cite Kolmogorov et al. 1991), at which size eddies break down due to kinematic viscosity of atmospheric constituents.could talk about DNS here A widespread technique when modeling the PBL is the use of large-eddy simulations (LES). Could discuss and include citations to fundamental

papers like Smagorinsky, Deardorff, etc. In LES, the equations of motion are filtered such that the largest, energy-containing eddies are explicitly resolved down to a grid resolution on the order of 10 meters. For eddies smaller than the resolution of the grid, sub-grid scale (SGS) parameterizations are used to represent the statistical attributes of unresolved eddies, including their energy dissipation and stress forces.

For simulation results presented in this thesis, we use the Weather Research and Forecasting model (WRF) configured for LES cite WRF. In practice, conducting LES studies in WRF arises from modeling choices including the representation of SGS turbulence parameterizations and adequately high grid resolution; that is, there is no "switch" for configuring WRF in LES mode, but rather structural choices which permit representation of the relevant dynamics.

3.1.1 Sub-grid scale parameterizations

A key choice in the implementation of LES is the selection of SGS turbulence parameterizations. Specifically, one must parameterize the SGS stress τ_{ij} and SGS flux q_i. The stress tensor τ_{ij} represents the deformational forces acting both normal ($i = j$) and perpendicular ($i \neq j$) to each grid cell, while the SGS flux q_i refers to the transport of scalars such as momentum, heat, or other quantities by unresolved eddies. A common technique for the closure of SGS stress and flux is the use of eddy-viscosity models. This technique was pioneered by Smagorinsky for parameterizing the motion of SGS eddies in a model of general circulation (Smagorinsky 1963). Eddy-viscosity models mimic the linear relationship between the stress tensor of a Newtonian fluid and shearing forces acting on the fluid scaled by the fluid's molecular viscosity. As such, eddy-viscosity models are not fundamentally grounded in physical tendencies of turbulent flows, but rather provide an empirical approximation that mimics Newtonian fluids and has been shown to be reasonable for representing SGS turbulence in modeling studies of the PBL cite?. The SGS stress and SGS flux are then expressed as

$$\tau_{ij} = -2\nu_T \tilde{S}_{ij}, \tag{3.1}$$

$$q_i = -\nu_\theta \frac{\partial \tilde{\theta}}{\partial x_i}, \tag{3.2}$$

where ν_T is the eddy viscosity coefficient, $\tilde{S}_{ij} = \frac{1}{2}(\partial \tilde{u}_i/\partial x_j + \partial \tilde{u}_j/\partial x_i)$ is the resolved strain rate tensor (i.e., the rate at which straining forces such as expansion and shearing due to resolved flow occur), ν_θ is the eddy diffusivity coefficient for some scalar quantity θ, and $\partial \tilde{\theta}/\partial x_i$ is the resolved-scale gradient of scalar θ

in direction x_i. As $\tilde{S}_{ij}$ and $\partial\tilde{\theta}/\partial x_i$ are known quantities determined at the resolved scale, eddy-diffusivity models then become a matter of determining ν_T and ν_θ.

Note to self, use Stoll in here somewhere? (Stoll et al. 2020)

Deardorff was the first to implement Smagorinsky's eddy-diffusivity SGS model for LES, however, he found that the model was overly diffusive for short wavelength features (Deardorff 1970). Deardorff 1980 instead proposed an alternative eddy-diffusivity model in which a prognostic equation for SGS kinetic energy E is solved alongside expressions for ν_T and ν_θ

$$\frac{\partial E}{\partial t} = -\frac{\partial \tilde{u}_j E}{\partial x_j} + 2\nu_T \tilde{S}_{ij}\tilde{S}_{ij} - \nu_\theta \frac{\partial \tilde{b}}{\partial z} + \frac{\partial}{\partial x_j} 2\nu_T \frac{\partial E}{\partial x_j} - \varepsilon, \tag{3.3}$$

$$\nu_T = C_1 \ell \sqrt{E}, \tag{3.4}$$

$$\nu_\theta = \left(1 + 2\frac{\ell}{\Delta}\right)\nu_T, \tag{3.5}$$

where b is buoyancy, ε is the turbulent kinetic energy (TKE) dissipation, C_1 is a coefficient that must be specified by the modeler, and ℓ is the turbulent length scale. Customarily, $C_1 = 0.1$ and we use this value as recommended by an idealized test case for LES simulations packaged alongside the WRF codebase.

3.1.2 Computational domain

We model the PBL in an 3D idealized domain with dimensions 10 km in both lateral dimensions and 2 km vertically. A horizontal resolution of 100 m was chosen alongside a vertical resolution of approximately 20 m[1], resulting in a domain of 100x100x100 grid cells. This resolution is necessary to resolve eddies responsible for turbulent transport in the PBL. A higher resolution vertically is desired in order to accurately represent vertical motions due to convective and turbulent transport. Time discretization is set to 1 second for all simulations, however sub-models such as chemistry (when active) further refine time discretization to maintain stability for integration.

The domain is absent of any topographic features with a uniform, flat surface what about surface roughness, etc?. Latitude and Longitude coordinates of (0, 0) are used internally for computing the solar zenith angle necessary for photolysis calculations, however, the domain's idealized topography is not intended to match the geographic region surrounding these coordinates.

[1]WRF uses a terrain-following pressure "eta" coordinate system for vertical levels. Note that because the domain only extends to 2 km vertically, vertical levels are nearly equally spaced apart.

3.1.3 Meteorological Initial Conditions

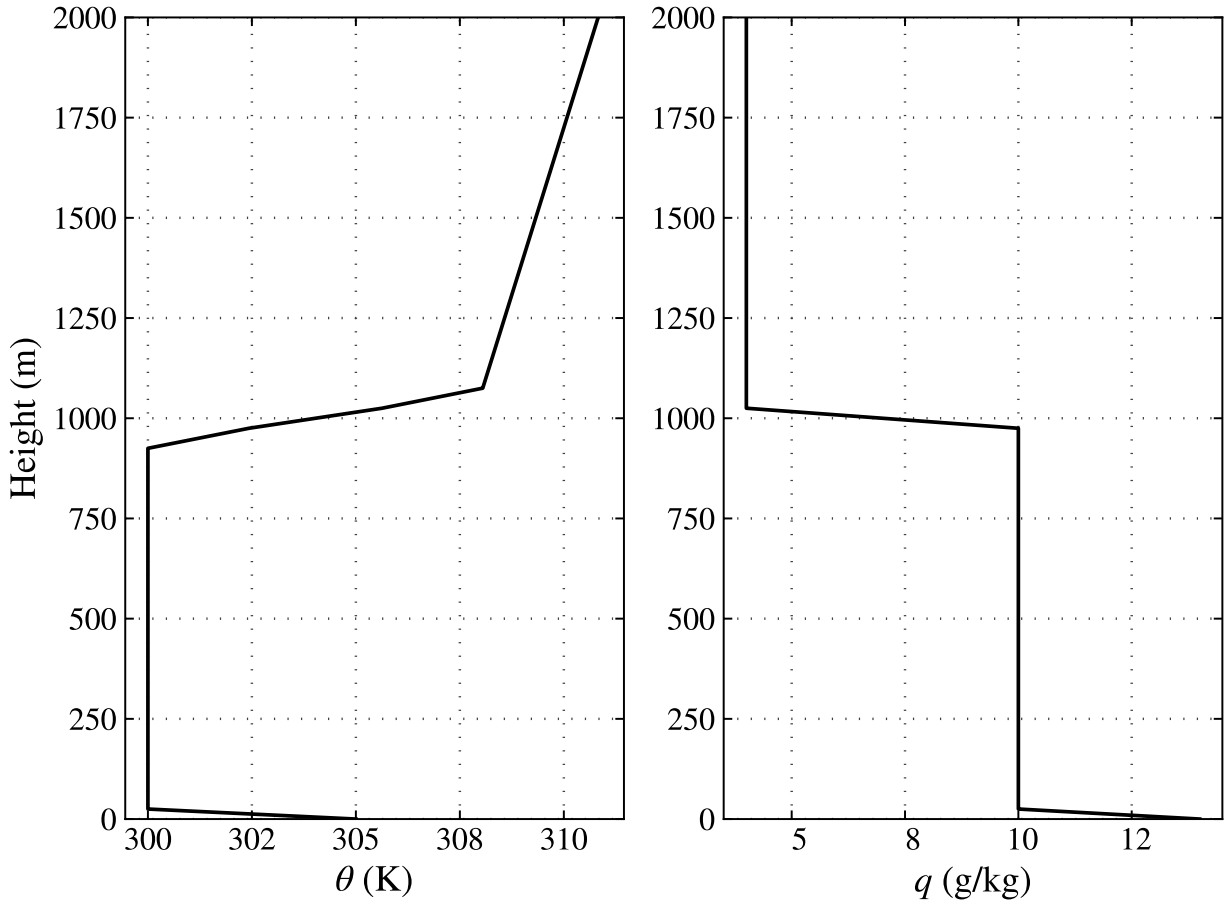

Figure 3.1: Idealized atmospheric sounding used for domain meteorological initial conditions. Initial conditions for potential temperature (left) and specific humidity (right). TODO: check what is best, units in brackets or in paretheses? Figure 3.2 uses brackets so I should be consistent either way...

The domain meteorological conditions are initialized using an ideal sounding typical of a convective boundary layer (see Figure 3.1). The lowest 25 m of the atmosphere are initially unstable to allow for parcels to rise due to buoyancy into the neutral PBL that extends to approximately 1 km. Above this point, the PBL is capped by an inversion up to 2 km.

Both zonal (u) and meridional (v) wind are set to zero throughout the entire domain. Tian et al. 2022 and Fast et al. 2019 both show that the impact of surface heterogeneities in surface heat fluxes on cloud formation and type are sensitive to wind conditions, and are most pronounced for minimal background winds. Extending the relevance of these findings to this thesis, our choice of an initial condition characterized by zero winds is intended to isolate the impact of emissions spatial heterogeneity on the evolving atmospheric

state of gasses and aerosols.

At the surface, the specific humidity q is highest at 14 $\mathrm{g\,kg^{-1}}$ and lowers to a uniform 10 g/kg within the PBL. Above the PBL, q is a uniform 4 $\mathrm{g\,kg^{-1}}$ extending vertically to the top of the domain. could also include plot of temperature and RH?. At the surface, a uniform surface heat flux (I assume sensible?) of 0.24 $\mathrm{K\,ms^{-1}}$ is set and random perturbations of the temperature field are imposed at the lowest four levels to initiate turbulence. The surface heat flux is responsible for maintaining convection and turbulent transport over the course of the simulation. Boundary conditions are periodic along all lateral boundaries.

3.1.4 Simulation spin-up

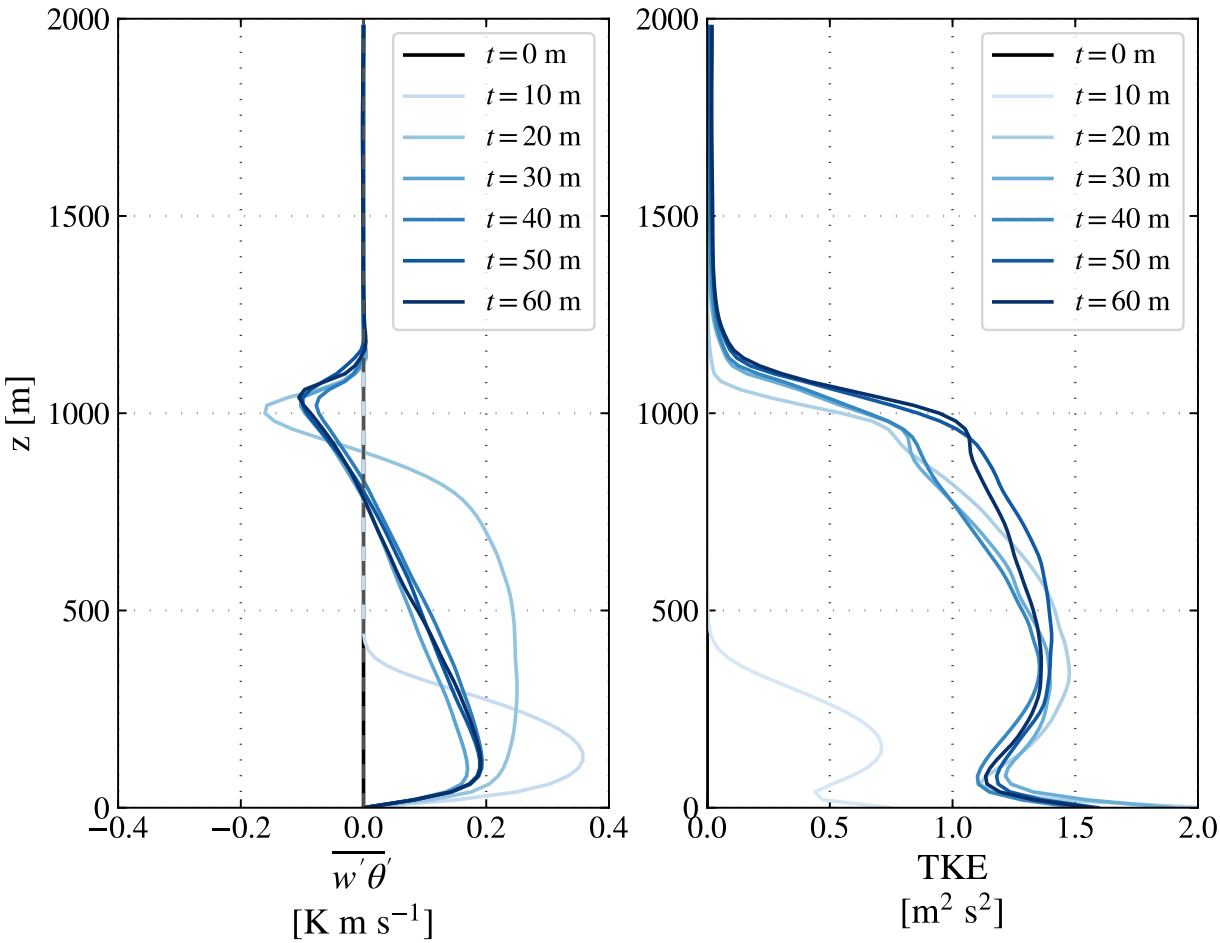

Figure 3.2: Resolved-scale vertical heat flux profiles (left) and TKE at intervals of 10 minutes during the first hour of simulation spin-up.

Prior to the release of gas and aerosol emissions, the simulation is allowed to spin up for a period of 1 hour.

During this time, convection and turbulence within the boundary become well established and throughly mix the initial conditions for gases and aerosols alongside transporting heat and momentum. In a well established convective boundary layer, the profile of vertical heat flux should decrease approximately linearly with height. Both resolved-scale[2] vertical heat flux and TKE profiles are shown in Figure 3.2 in increments of 10 minutes from $t = 0$ minutes to $t = 1$ hour. Initially, vertical heat flux is zero everywhere due to the initial condition of zero vertical velocity. At $t = 10$ minutes, vertical heat flux is localized near the surface and exceeds 0.3 $\mathrm{K\,m\,s^{-1}}$. By $t = 30$ minutes, initial transient behavior in vertical heat flux relaxes as the convective boundary layer becomes more well established and the heat flux profile takes on a linearly decreasing trend with height. Profiles for subsequent times agree closely with the profile at $t = 30$ minutes, indicating that the convective boundary layer is near fully established by 30 minutes. Note that the TKE profiles in Figure 3.2 indicate that energy-containing eddies in the upper boundary layer continue to develop through $t = 1$ hour, as TKE increases in the upper boundary layer from ~ 0.7 $\mathrm{m^2\,s^2}$ at $t = 30$ minutes to ~ 1.1 $\mathrm{m^2\,s^2}$ by $t = 1$ hour. Thus 1 hour of model spin-up time was chosen to adequately allow for development of the convective boundary layer and resolved scales of turbulence.

3.2 Gas phase simulations

3.2.1 Chemical mechanism

In Chapter 4, we conduct simulations with only gas phase initial conditions and emissions to isolate the impact of emissions spatial heterogeneity on gas phase reactions. For these simulations, we use WRF version 4.4.1. Beginning with WRF version 4, various sub-models including chemical mechanisms are packaged alongside the WRF codebase. We select the chemical mechanism Carbon-Bond Mechanism-Z (CBMZ) for gas phase photochemical reactions (Zaveri and Peters 1999). CBMZ models both inorganic and organic compounds prevalent in anthropogenic and biogenic emissions. CBMZ allows computationally efficient calculation of over 100 reactions across dozens of chemical species. This is possible due to the model's "lumped-structure" approach to sorting similar organic compounds by their carbon bond structure (e.g, alkanes, carbonyls, etc.). This reduces the need for tracking large volumes of organic species and reactions. Despite simplifications to the organic chemistry mechanism, CBMZ has been shown to accurately

[2]Ideally, one would evaluate total (resolved + parameterized) vertical heat flux and total TKE. WRF does not provide output for SGS quantities, so it would be necessary for one to modify the codebase to allow exporting these additional data.

represent concentrations of compounds of primary interest for atmospheric chemistry applications (e.g., O_3, NO_x, etc.) (Zaveri and Peters 1999, other citations?).

3.2.2 Initial conditions and emissions

Table 3.1: Gas phase emissions and initial conditions. Table taken from N. Riemer et al. 2009 with permission.

Species	Symbol	Initial Mole Fraction (ppb)	Emissions (nmol m^{-2} s^{-1})
Nitric oxide	NO	0.1	31.8
Nitrogen dioxide	NO_2	1.0	1.67
Nitric acid	HNO_3	1.0	
Ozone	O_3	50.0	
Hydrogen peroxide	H_2O_2	1.1	
Carbon monoxide	CO	21	291.3
Sulfur dioxide	SO_2	0.8	2.51
Ammonia	NH_3	0.5	6.11
Hydrogen chloride	HCl	0.7	
Methane	CH_4	2200	
Ethane	C_2H_6	1.0	
Formaldehyde	HCHO	1.2	1.68
Methanol	CH_3OH	0.12	0.28
Methyl hydrogen peroxide	CH_3OOH	0.5	
Acetaldehyde	ALD2	1.0	0.68
Paraffin carbon	PAR	2.0	96
Acetone	AONE	1.0	1.23
Ethene	ETH	0.2	7.2
Terminal olefin carbons	OLET	$2.3 \cdot 10^{-2}$	2.42
Internal olefin carbons	OLEI	$3.1 \cdot 10^{-4}$	2.42
Toluene	TOL	0.1	4.04
Xylene	XYL	0.1	2.41
Lumped organic nitrate	ONIT	0.1	
Peroxyacetyl nitrate	PAN	0.8	
Higher organic acid	RCOOH	0.2	
Higher organic peroxide	ROOH	$2.5 \cdot 10^{-2}$	
Isoprene	ISOP	0.5	0.23
Alcohols	ANOL		3.45

Gas phase initial conditions and emissions are chosen to represent species and concentrations typical of an urban plume and are adopted from N. Riemer et al. 2009. The authors determined gas phase concentrations and emission rates via the 1987 Southern California Air Quality Study (SCAQS) data set which contains measurements of both gas phase species and particulate matter mass concentrations collected at multiple sites

across the Los Angeles basin (Zaveri, Easter, et al. 2008). Table 3.1 contains all gas phase initial conditions and emission rates Note if I didnt end up using some of these species then remove those. Empty entries signify zero concentrations or emission rates. To allow for simulation spin-up, all emission rates are set zero during the first hour of simulations. Subsequently, emitted compounds are released only at the surface and at a constant rate as specified in Table 3.1 for the remainder of the simulation.

3.3 Multiphase simulations

3.3.1 Chemical mechanism

Chapter 5 presents simulation results where both gas phase chemistry and aerosol processes (e.g., coagulation, gas-particle partitioning, etc.) are modeled. Both gas phase and aerosol chemistry is represented using the Model for Simulating Aerosol Interactions and Chemistry (MOSAIC) (Zaveri, Easter, et al. 2008). MOSAIC was developed by the authors of CBMZ, and it should be noted that CBMZ is included a sub-model within MOSAIC for handling gas phase chemistry. For aerosol chemistry, MOSAIC simulates dynamic gas-particle partitioning and phase-dependent thermodynamic equilibrium. A key challenge for modeling aerosol chemistry is that the coupled system of solid-liquid phase reactions that govern aerosol thermodynamic equilibrium is often numerically stiff due to the rate of reactions varying over large timescales. Often, chemical mechanisms solve such stiff systems in a computationally expensive manner either by iterative techniques or by directly minimizing the Gibbs Free energy of the system. MOSAIC takes an alternative approach whereby the system of equilibrium reactions is reformulated as a pseudo-transient system. This recasts the system as ordinary differential equations, for which standard numerical techniques are used to integrate and obtain equilibrium steady state solutions. This approach makes MOSAIC computationally efficient while maintaining good agreement when benchmarked against numerically rigorous and accurate models (Zaveri, Easter, et al. 2008).

3.3.2 Aerosol representation

We use the Particle Monte Carlo (PartMC) model for particle-resolved representation of aerosols (N. Riemer et al. 2009). In PartMC, aerosol particles are represented via a set of computational particles with appropriate multiplicity to represent the desired aerosol population. Each computational particle is allowed to compositionally vary due to aerosol processes (e.g., coagulation, condensation, gas-particle partitioning, etc.), thus

allowing the representation of a far greater degree of compositional diversity and aerosol properties than sectional or modal based aerosol models citations. PartMC is a box model, meaning that within computational grid cells, the position of computational particles is not tracked. Instead, processes such as coagulation are handled in the probabilistic manner of Gillepsi 1975. PartMC is coupled with MOSAIC, thereby leveraging the computational efficiency and accuracy of each model in allowing full representation of an aerosol state (number and mass concentration, per-particle composition) under aging due to both aerosol physical processes and chemical reactions.

Curtis, Nicole Riemer, and West 2017 coupled PartMC-MOSAIC with WRF for a single column model of the planetary boundary layer. The authors developed approaches for modeling the turbulent diffusion and dry deposition of aerosol particles as stochastic processes. The resulting modeling framework, WRF-PartMC-MOSAIC, is extended here for use with 3D LES.

For WRF-PartMC-MOSAIC-LES, we use 100 computational particles per grid cell for a total of 100 million computational particles throughout the domain at initialization. This value was chosen to balance computational efficiency and storage demands alongside numerical representability – too few computational particles will result in random noise for aerosol population properties due to the stochastic nature of the PartMC model.

3.3.3 Initial conditions and emissions

Initial conditions and emissions of gas phase species match those discussed in Section 3.2.2 and are displayed in Table 3.1. Similarly, aerosol initial conditions and emission rates are adopted from N. Riemer et al. 2009, who based aerosol distributions, composition, and emission rates off measurements collected as part of the SCAQS campaign in the Los Angeles valley. Aerosol initial conditions and emission properties are summarized in Table 3.2. Size distributions for aerosol initial conditions and emissions are shown in Figure 3.3 and Figure 3.4, respectively. The aerosol initial condition is comprised of two modes, including a Aitken mode and accumulation mode. Each mode is an equal mixture of 50% ammonium sulfate and 50% primary organic aerosol (POA). Three emission modes are chosen to represent emissions from various urban combustion sources, including cooking, diesel vehicles, and gasoline vehicles. The cooking emission mode is comprised of 100% POA and the diesel and gasoline modes are each a mixture of POA and black carbon (BC).

Table 3.2: Aerosol emissions and initial conditions. Table taken from N. Riemer et al. 2009 with permission.

Initial/Background	N (m^{-3})	D_{gn} (μm)	σ_g	Composition by Mass
Aitken Mode	$3.2 \cdot 10^9$	0.02	1.45	50% $(NH_4)_2SO_4$, 50% POA
Accumulation Mode	$2.9 \cdot 10^9$	0.116	1.65	50% $(NH_4)_2SO_4$, 50% POA
Emissions	E (m^{-2} s^{-1})	D_{gn} (μm)	σ_g	Composition by Mass
Meat cooking	$9 \cdot 10^6$	0.086	1.9	100% POA
Diesel vehicles	$1.6 \cdot 10^8$	0.05	1.7	30% POA, 70% BC
Gasoline vehicles	$5 \cdot 10^7$	0.05	1.7	80% POA, 20% BC

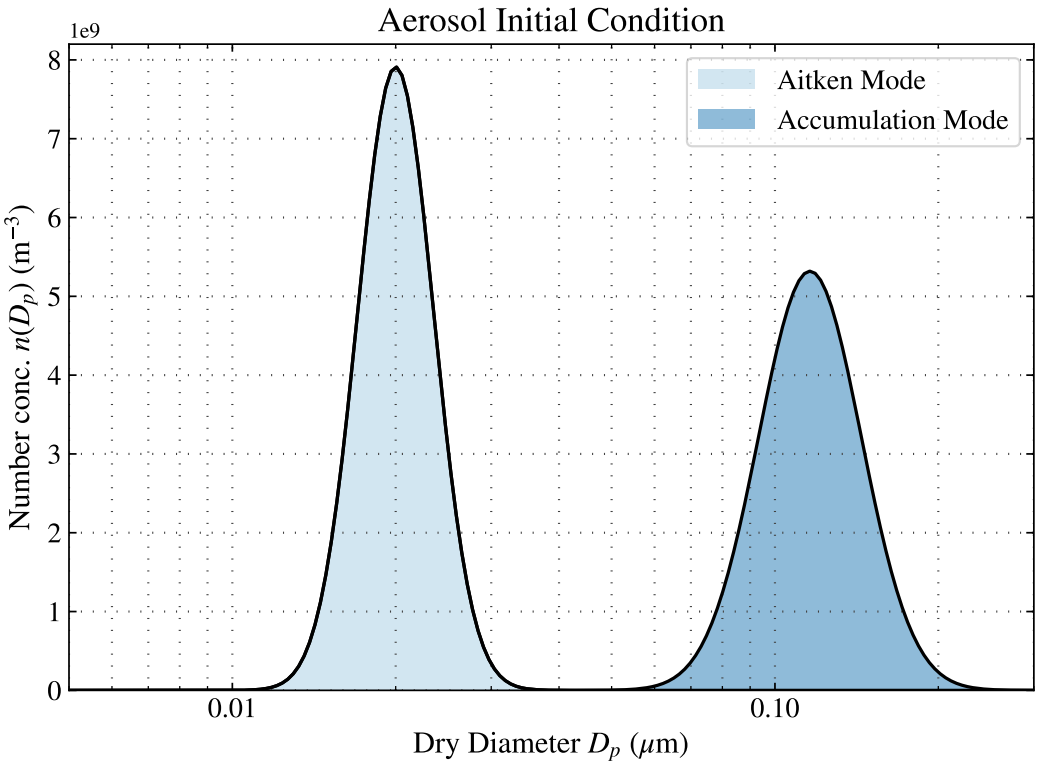

Figure 3.3: Aerosol initial condition size distributions.

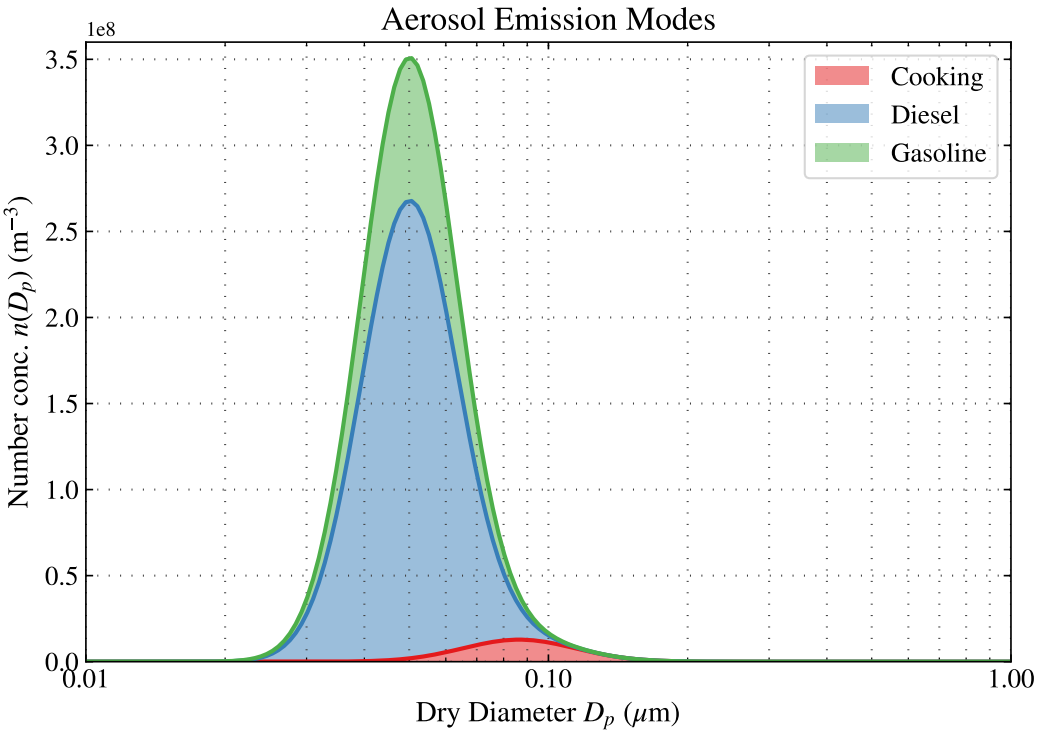

Figure 3.4: Aerosol emission size distributions.

Chapter 4

Impacts of emissions spatial heterogeneity on gas-phase reactions

Chapter 5

Impacts of emissions spatial heterogeneity on aerosol properties in a particle resolved framework

Chapter 6

Conclusions

References

Cooper, Scott D. et al. (Mar. 1997). "Quantifying Spatial Heterogeneity in Streams". In: *Journal of the North American Benthological Society* 16.1. Publisher: The University of Chicago Press, pp. 174–188. ISSN: 0887-3593. DOI: 10.2307/1468250. URL: https://www-journals-uchicago-edu.proxy2.library.illinois.edu/doi/10.2307/1468250 (visited on 05/09/2024).

Curtis, Jeffrey H., Nicole Riemer, and Matthew West (Nov. 2017). "A single-column particle-resolved model for simulating the vertical distribution of aerosol mixing state: WRF-PartMC-MOSAIC-SCM v1.0". English. In: *Geoscientific Model Development* 10.11. Publisher: Copernicus GmbH, pp. 4057–4079. ISSN: 1991-959X. DOI: 10.5194/gmd-10-4057-2017. URL: https://gmd.copernicus.org/articles/10/4057/2017/ (visited on 10/06/2022).

Damköhler, Gerhard (Apr. 1947). "The Effect of Turbulence on the Flame Velocity in Gas Mixtures". en. In: *Zeitschrift fuer Elektrochemie und Angewandte Physikalische Chemiw* 46.11. Number: NACA-TM-1112. URL: https://ntrs.nasa.gov/citations/20050009802 (visited on 06/08/2023).

Danckwerts, P. V. (July 1952). "The definition and measurement of some characteristics of mixtures". en. In: *Applied Scientific Research, Section A* 3.4, pp. 279–296. ISSN: 1573-1987. DOI: 10.1007/BF03184936. URL: https://doi.org/10.1007/BF03184936 (visited on 06/08/2023).

Deardorff, James W. (Apr. 1970). "A numerical study of three-dimensional turbulent channel flow at large Reynolds numbers". en. In: *Journal of Fluid Mechanics* 41.2, pp. 453–480. ISSN: 1469-7645, 0022-1120. DOI: 10.1017/S0022112070000691. URL: https://www.cambridge.org/core/journals/journal-of-fluid-mechanics/article/numerical-study-of-threedimensional-turbulent-channel-flow-at-large-reynolds-numbers/D84769F4A3443E4C87E8878303890999 (visited on 05/18/2024).

— (June 1980). "Stratocumulus-capped mixed layers derived from a three-dimensional model". In: *Boundary-Layer Meteorology* 18.4, pp. 495–527. ISSN: 1573-1472. DOI: 10.1007/BF00119502. URL: https://doi.org/10.1007/BF00119502.

Dong, Pinliang (June 2000). “Lacunarity for Spatial Heterogeneity Measurement in GIS”. In: *Geographic Information Sciences* 6.1. Publisher: Taylor & Francis _eprint: https://doi.org/10.1080/10824000009480530, pp. 20–26. ISSN: 1082-4006. DOI: 10.1080/10824000009480530. URL: https://doi.org/10.1080/10824000009480530 (visited on 05/09/2024).

Fast, Jerome D. et al. (2019). “The Impact of Variable Land-Atmosphere Coupling on Convective Cloud Populations Observed During the 2016 HI-SCALE Field Campaign”. en. In: *Journal of Advances in Modeling Earth Systems* 11.8. _eprint: https://onlinelibrary.wiley.com/doi/pdf/10.1029/2019MS001727, pp. 2629–2654. ISSN: 1942-2466. DOI: 10.1029/2019MS001727. URL: https://onlinelibrary.wiley.com/doi/abs/10.1029/2019MS001727 (visited on 10/06/2022).

Loke, Lynette H. L. and Ryan A. Chisholm (2022). “Measuring habitat complexity and spatial heterogeneity in ecology”. en. In: *Ecology Letters* 25.10. _eprint: https://onlinelibrary.wiley.com/doi/pdf/10.1111/ele.14084, pp. 2269–2288. ISSN: 1461-0248. DOI: 10.1111/ele.14084. URL: https://onlinelibrary.wiley.com/doi/abs/10.1111/ele.14084 (visited on 05/09/2024).

Plexida, Sofia G. et al. (Feb. 2014). “Selecting landscape metrics as indicators of spatial heterogeneity—A comparison among Greek landscapes”. In: *International Journal of Applied Earth Observation and Geoinformation* 26, pp. 26–35. ISSN: 1569-8432. DOI: 10.1016/j.jag.2013.05.001. URL: https://www.sciencedirect.com/science/article/pii/S0303243413000500 (visited on 05/10/2024).

Riemer, N. et al. (2009). “Simulating the evolution of soot mixing state with a particle-resolved aerosol model”. en. In: *Journal of Geophysical Research: Atmospheres* 114.D9. _eprint: https://onlinelibrary.wiley.com/doi/pdf/10.1029/200 ISSN: 2156-2202. DOI: 10.1029/2008JD011073. URL: https://onlinelibrary.wiley.com/doi/abs/10.1029/2008JD011073 (visited on 10/06/2022).

Seinfeld, J and S Pandis (1998). *Atmospheric Chemistry and Physics: From Air Pollution to Climate Change*.

Shu, Hua et al. (July 2019). “Quantifying the spatial heterogeneity of points”. In: *International Journal of Geographical Information Science* 33.7. Publisher: Taylor & Francis _eprint: https://doi.org/10.1080/13658816.2019.1577432, pp. 1355–1376. ISSN: 1365-8816. DOI: 10.1080/13658816.2019.1577432. URL: https://doi.org/10.1080/13658816.2019.1577432 (visited on 05/09/2024).

Smagorinsky, J. (Mar. 1963). “GENERAL CIRCULATION EXPERIMENTS WITH THE PRIMITIVE EQUATIONS: I. THE BASIC EXPERIMENT”. EN. In: *Monthly Weather Review* 91.3. Publisher: American Meteorological Society Section: Monthly Weather Review, pp. 99–164. ISSN: 1520-0493, 0027-0644. DOI: 10.1175/1520-0493(1963)091<0099:GCEWTP>2.3.CO;2. URL: https:

//journals.ametsoc.org/view/journals/mwre/91/3/1520-0493_1963_091_0099_gcewtp_2_3_co_2.xml (visited on 05/16/2024).

Stoll, Rob et al. (Dec. 2020). "Large-Eddy Simulation of the Atmospheric Boundary Layer". en. In: *Boundary-Layer Meteorology* 177.2, pp. 541–581. ISSN: 1573-1472. DOI: 10.1007/s10546-020-00556-3. URL: https://doi.org/10.1007/s10546-020-00556-3 (visited on 10/06/2022).

Thiffeault, Jean-Luc (Jan. 2012). "Using multiscale norms to quantify mixing and transport". en. In: *Nonlinearity* 25.2, R1. ISSN: 0951-7715. DOI: 10.1088/0951-7715/25/2/R1. URL: https://dx.doi.org/10.1088/0951-7715/25/2/R1 (visited on 05/31/2023).

Tian, Jingjing et al. (2022). "How Does Land Cover and Its Heterogeneity Length Scales Affect the Formation of Summertime Shallow Cumulus Clouds in Observations From the US Southern Great Plains?" en. In: *Geophysical Research Letters* 49.7. _eprint: https://onlinelibrary.wiley.com/doi/pdf/10.1029/2021GL097070, e2021GL097070. ISSN: 1944-8007. DOI: 10.1029/2021GL097070. URL: https://onlinelibrary.wiley.com/doi/abs/10.1029/2021GL097070 (visited on 05/31/2023).

Vinuesa, Jean-François and Jordi Vilá-Guerau De Arellano (Dec. 2003). "Fluxes and (co-)variances of reacting scalars in the convective boundary layer". In: *Tellus B: Chemical and Physical Meteorology* 55.4. Publisher: Taylor & Francis _eprint: https://doi.org/10.3402/tellusb.v55i4.16382, pp. 935–949. ISSN: null. DOI: 10.3402/tellusb.v55i4.16382. URL: https://doi.org/10.3402/tellusb.v55i4.16382 (visited on 03/06/2024).

Zaveri, Rahul A., Richard C. Easter, et al. (2008). "Model for Simulating Aerosol Interactions and Chemistry (MOSAIC)". en. In: *Journal of Geophysical Research: Atmospheres* 113.D13. _eprint: https://onlinelibrary.wiley.com/doi/pd ISSN: 2156-2202. DOI: 10.1029/2007JD008782. URL: https://onlinelibrary.wiley.com/doi/abs/10.1029/2007JD008782 (visited on 10/06/2022).

Zaveri, Rahul A. and Leonard K. Peters (1999). "A new lumped structure photochemical mechanism for large-scale applications". en. In: *Journal of Geophysical Research: Atmospheres* 104.D23. _eprint: https://onlinelibrary.wiley.com/doi/pdf/10.1029/1999JD900876, pp. 30387–30415. ISSN: 2156-2202. DOI: 10.1029/1999JD900876. URL: https://onlinelibrary.wiley.com/doi/abs/10.1029/1999JD900876 (visited on 07/13/2023).